MANNGA Deliverable

D3.1 Report on phenomenological modelling of CMLGs, accompanied by a code for the models' implementation, a summary of its validation against micromagnetic results, and a summary of examples of its application to physical devices, including their forecasted KPIs.

Version 1.0

Grant Agreement number	101070347
Action Acronym	MANNGA
Action Title	MAGNONIC ARTIFICIAL NEURAL NETWORKS AND GATE ARRAYS
Call	HORIZON-CL4-2021-DIGITAL-EMERGING-01
Version date of the Annex I against which the assessment will be made	31.5.2022
Start date of the project	1.9.2022
Due date of the deliverable	29.02.2024
Actual date of submission	05.04.2024
Lead BEN / AP for the deliverable	UNEXE
Dissemination level of the deliverable	Public

Coordinator, PI
Sebastiaan van Dijken
AALTO KORKEAKOULUSÄÄTIÖ SR, Aalto University School of Science

Scientific coordinator
Volodymyr Kruglyak
THE UNIVERSITY OF EXETER

Co-funded by the European Union

Funded by the European Union (GA No. 101070347). Views and opinions expressed are however those of the author(s) only and do not necessarily reflect those of the European Union or the European Health and Digital Executive Agency (HADEA). Neither the European Union nor the granting authority can be held responsible for them.

Authors in alphabetical order		
Name	Beneficiary	e-mail
Kevin Fripp	The University of Exeter (UNEXE)	K.G.Fripp@exeter.ac.uk
Volodymyr Kruglyak	The University of Exeter (UNEXE)	V.V.Kruglyak@exeter.ac.uk
Andrey Shytov	The University of Exeter (UNEXE)	A.Shytov@exeter.ac.uk

Document reviewers		
Name	Beneficiary	e-mail
Sebastiaan van Dijken	Aalto University	Sebastiaan.van.dijken@aalto.fi
Georg Schmidt	Martin Luther University Halle-Wittenberg	georg.schmidt@physik.uni-halle.de

Executive summary

This deliverable reports on MANNGA's design of chiral magnonic logic gates (CMLGs) and their modelling using micromagnetic simulations and an upgraded version of our phenomenological model previously developed to describe and to predict properties of different types of magnonic resonators (reported in MANNGA's previous deliverable D2.3). The current version of the model is valid for isolated CMLGs, while its generalisation to arrays of those is under way.

Contents

1. Introduction: The aims and objects of the phenomenological modelling in T3.1

This deliverable results from activities in MANNGA's Task T3.1, which aims to design chiral magnonic logic gates (CMLGs) and create their phenomenological models, validating the designs using micromagnetic simulations. In contrast to similar activities in the beginning of the project, the designs and models are (i) informed by the existing experimental data obtained from MANNGA's current designs of magnonic resonators, rather than complete CMLGs; and (ii) intended to be used in experimental implementation of the designed CMLGs. MANNGA's current designs of magnonic resonators exploit Fabry-Pérot resonances [1] formed due to spin wave (SW) reflection from magnonic dispersion mismatches at interfaces between yttrium-iron garnet (YIG) regions with and without a metallic magnetic overlayer; the structures are called here magnonic Fabry-Pérot resonators (MFPRs). In MANNGA, we have established that the incident SW energy is resonantly concentrated in the YIG region under the overlayer [2], and the energy concentration leads to an enhanced nonlinear response to the excitation. The response is still, however, described well by our model developed for the case of energy concentration in the overlayer itself in chiral magnonic resonators (CMRs) from [3].

2. Brief description of the basic CMLG designs.

The basic design of a CMLG is shown schematically in Fig. 1. The design uses a single CMR or MFPR as a nonlinear element. Two SW inputs 'A' and 'B' are assumed to be combined into a single signal using an external circuit, and an additional control signal 'P' is used to replenish the signal's energy, so as to enable concatenation of multiple gates.

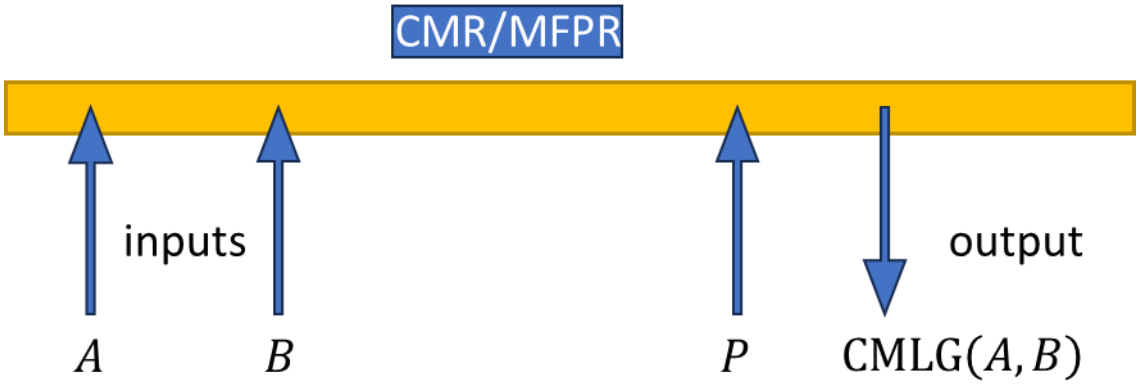

Figure 1. The basic CMLG design is schematically shown: A and B are the two SW inputs, and C is the control signal. The resonator 'CMR/MFPR', which can be either a CMR, or MFPR, acts nonlinearly on the superposition of A and B. The output of the CMLG is then denoted as CMLG(A,B).

Under different assumptions about the amplitudes and phases of A, B, and P, the device from Fig. 1 can perform different logical functions, such as 'AND' and 'NAND' gates (shown in Figs. 2 and 3, respectively) built assuming parameters of a CMR from [3] and $\mathrm{CMLG}(A,B) \approx P + \mathrm{CMR}(A+B)$.

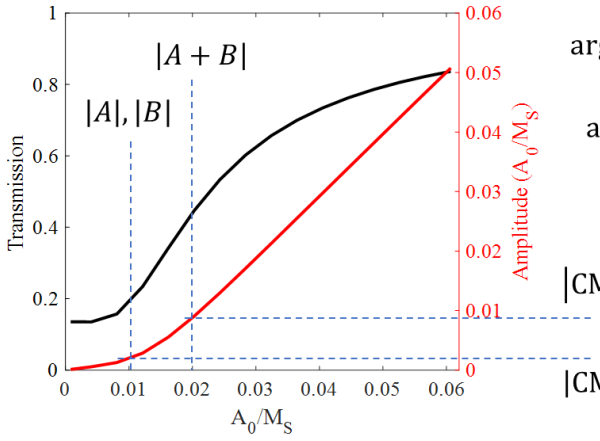

$$\arg\left(\mathrm{CMR}_{\mathrm{high}}(A+B)\right) \gtrsim \frac{3\pi}{2} + \arg(A+B)$$

$$\arg\left(\mathrm{CMR}_{\mathrm{low}}(A+B)\right) \approx \pi + \arg(A+B)$$

$$\left|\mathrm{CMR}_{\mathrm{high}}(A+B)\right|$$

$$\left|\mathrm{CMR}_{\mathrm{low}}(A+B)\right|$$

AND gate truth table		
Input		Output
A	B	A **AND** B
0	0	0
0	1	0
1	0	0
1	1	1

Assume:

$$\arg(A+B) \approx \arg(A) \approx \arg(B)$$

$$\arg\left(\mathrm{CMR}_{\mathrm{low}}(A+B)\right) \approx \pi + \arg(A+B)$$

$$|P| \approx \left|\mathrm{CMR}_{\mathrm{low}}(A+B)\right|$$

$$\arg(P) \approx \pi + \arg\left(\mathrm{CMR}_{\mathrm{low}}(A+B)\right)$$

Figure 2. The CMLG design from Fig.1 performing 'AND' function.

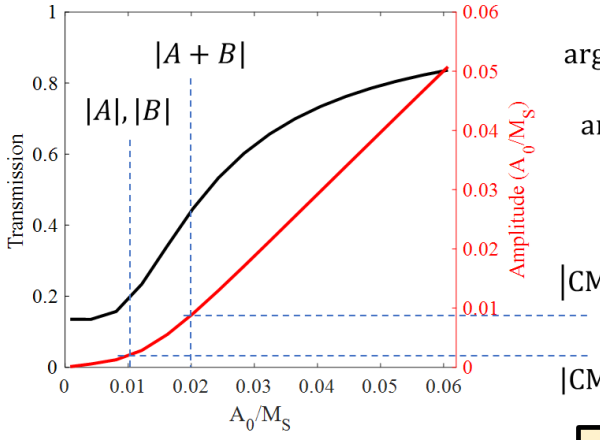

$$\arg\left(\mathrm{CMR}_{\mathrm{high}}(A+B)\right) \approx -\frac{\pi}{4} + \arg(A+B)$$

$$\arg\left(\mathrm{CMR}_{\mathrm{low}}(A+B)\right) \approx \arg(A+B)$$

$$\left|\mathrm{CMR}_{\mathrm{high}}(A+B)\right|,$$

$$\left|\mathrm{CMR}_{\mathrm{low}}(A+B)\right|,$$

NAND gate truth table		
Input		Output
A	B	A **NAND** B
0	0	1
0	1	1
1	0	1
1	1	0

Assume:

$$\arg(A+B) \approx \arg(A) \approx \arg(B)$$

$$\arg\left(\mathrm{CMR}_{\mathrm{low}}(A+B)\right) \approx \arg(A+B)$$

$$|P| \approx \left|\mathrm{CMR}_{\mathrm{high}}(A+B)\right|$$

$$\arg(P) \approx \pi + \arg\left(\mathrm{CMR}_{\mathrm{high}}(A+B)\right)$$

Figure 3. The CMLG design from Fig.1 performing 'NAND' function.

3. Brief description of the phenomenological model.

In reality, the assumption of $\mathrm{CMLG}(A,B) \approx P + \mathrm{CMR}(A+B)$ and so the functions illustrated in Figs. 2&3 would not necessarily hold (e.g. due to peculiarities of injecting the control signal 'P'), while the design shown in Fig. 1 could be modified by injecting 'P' in different places. Hence, our phenomenological model was implemented under a more general set of assumptions, illustrated in Fig.4.

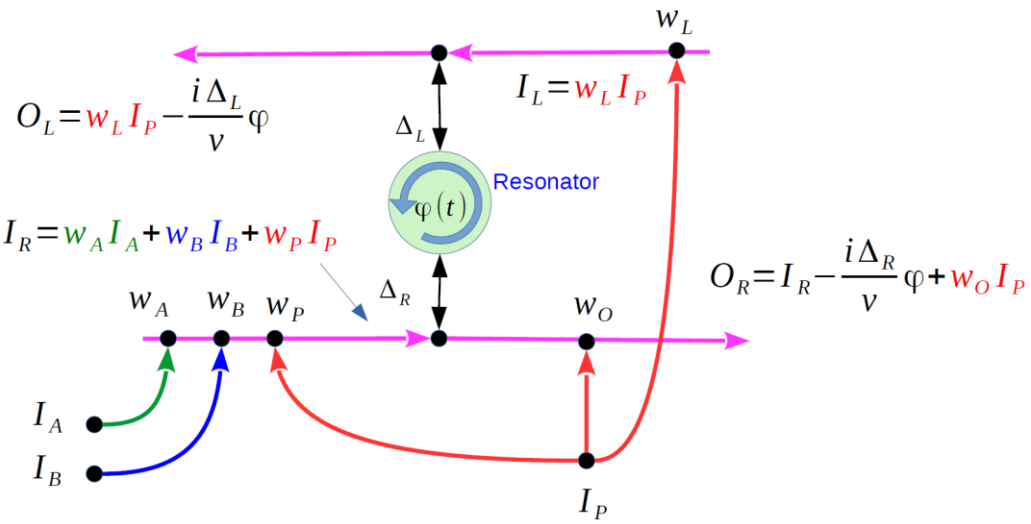

Figure 4. The system captured by the phenomenological model is schematically shown.

As before, the device is driven by three signals, two logical ones I_A, I_B, and a control one I_P, while the complex-valued weights w_A, w_B, w_P, and w_O, and w_L describe how these inputs are injected into different channels of the device. In particular, the design from Fig. 1 is obtained by setting $A = w_A I_A$, $B = w_B I_B$, $P = w_O I_P$, and $w_P = w_L = 0$. The right- and left-moving SWs incident on the resonator are given by I_R and I_L, respectively, while quantities O_R and O_L describe the output of and the SW reflected by the device, respectively. Quantities Δ_R and Δ_L describe coupling of I_R and I_L, respectively, to the resonator's mode $\varphi(t)$. The latter is the only non-linear element of the device, and its nonlinearity is described using the method developed in MANNGA's WP2, described in [3], and presented (with validation against micromagnetic simulation and experiment for isolated MFPRs) in deliverable D2.3. The developed phenomenological mode is implemented within a Python code, which is available from https://github.com/avshytov/MANNGA-Spin-Wave-Scattering. Expectedly, the code runs drastically faster and has a reduced memory footprint as compared to full micromagnetic simulations. However, full exploration of the parameter space captured by the model still represents a challenge, with some examples shown in the next section.

4. Examples of using the phenomenological model.

To illustrate the use of the model, we apply to the magnonic NAND gate based on a resonator with a transmission characteristic shown in Fig. 5. Based on this, we can choose a working frequency () and specific logic threshold values, e.g. 0.0 < LOW < 0.035, 0.045 < HIGH <0.08. Requiring that both the

inputs and the output of the device adhere to these definitions, we define a performance metric ('ANTI-SCORE') by calculating the area (number of discrete points) in which the output fails to be within the expected limits, i.e. is invalid. So, the smaller is the metric, the better performance of the gate. The optimisation is then performed via differential evolution, with complex weights, and examples of the results are shown in the following sections.

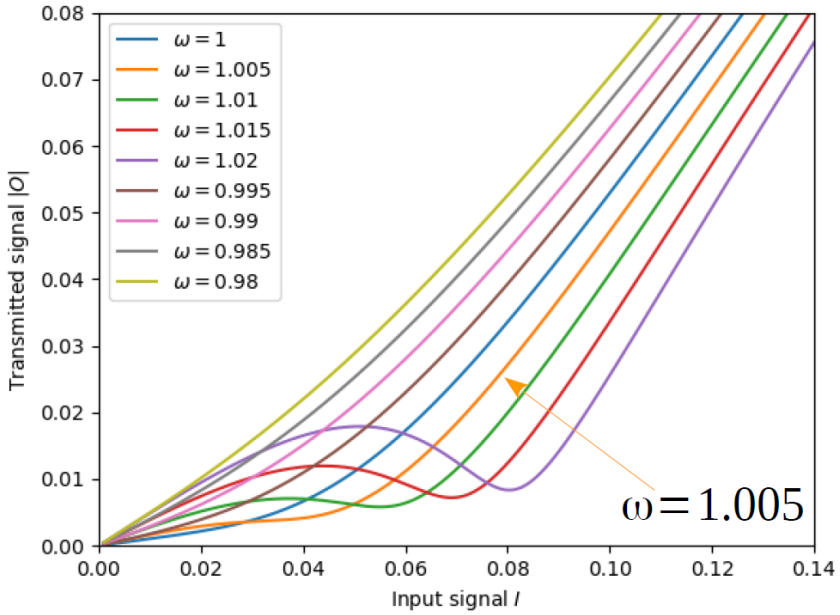

Figure 5. The signal transmitted by a resonator used in the calculations is shown for different frequencies of the incident SW, stated in arbitrary units. The frequency of $\omega = 1.001$ is used in the subsequent analysis.

4.1 Optimisation of a NAND gate.

We begin by showing results of optimisation for a magnonic NAND gate. Figure 6 is obtained under assumption of equal weight for the logic inputs, $w_A = w_B$. We see that the output depends on the combination $w_A I_A + w_B I_B$ and the output plot has a diagonal character, preventing us from obtaining an ANTI-SCORE smaller than 588 (out of 10,000). So, Figure 6 tests an assumption of orthogonal phases of the logic inputs, $iw_A = w_B$. We see that the "diagonality" is suppressed, and the ANTI-SCORE is reduced to 472.

$$w_A = w_B = 0.977679, \quad w_P = -0.166609 - 0.112921\,i$$
$$w_L = -0.077261 + 0.360543\,i, \quad w_O = -0.362986 - 0.585067\,i$$

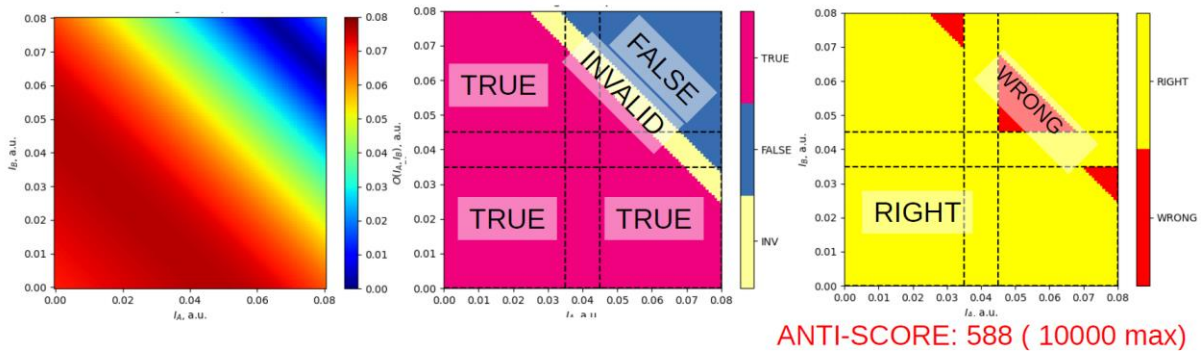

Figure 6. Result of optimisation of the NAND gate for the case of identical input weights.

$$w_A = 0.995342, \quad w_B = i\,w_A, \quad w_P = -0.795799 + 0.364510\,i$$
$$w_L = -0.795432 + 0.697910\,i, \quad w_O = 0.3651983 - 0.011628\,i$$

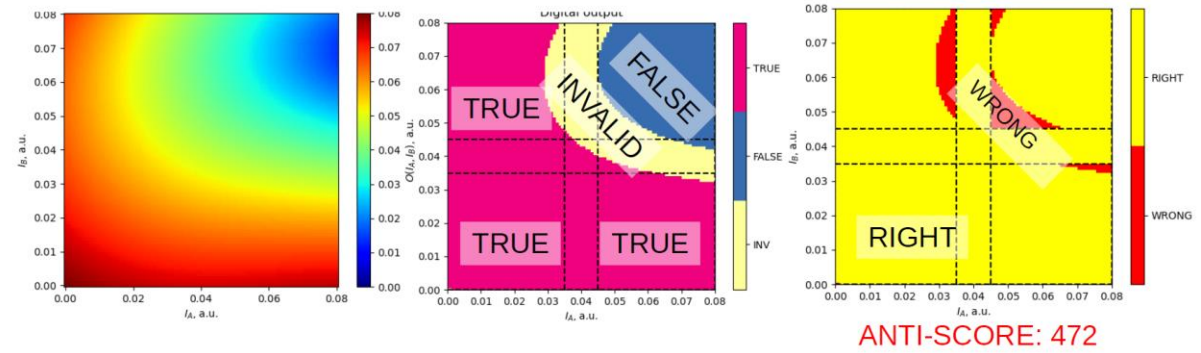

Figure 7. Result of optimisation of the NAND gate for the case of input weights phase-shifted by 90°.

4.2 Optimisation of an AND gate.

Figure 8 presents results of optimisation for an AND gate for the case of identical input weights. The result is noticeably worse than that for the NAND gate and cannot be improved by assuming phase-shifted input weights.

$$w_A = w_B = 0.777200, \quad w_P = 0.230858 + 0.129826\,i$$
$$w_L = 0.0194796 - 0.080664\,i, \quad w_O = 0.110167 - 0.285284\,i$$

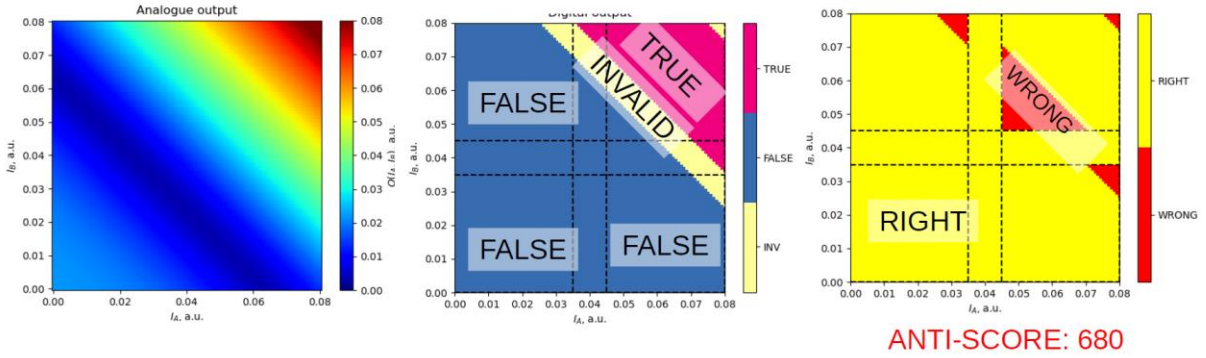

Figure 8. Result of optimisation of the AND gate for the case of identical input weights.

4.3 Optimisation of a NOR gate.

Figure 9 presents results of optimisation for an NOR gate for the case of identical input weights. Again, the result is noticeably worse than that for the NAND gate and cannot be improved by assuming phase-shifted input weights.

$$w_A = w_B = 0.588207, \quad w_P = 0.758876 - 0.441503\,i$$
$$w_L = 0.679213 + 0.681189\,i, \quad w_O = -0.368094 - 0.680920\,i$$

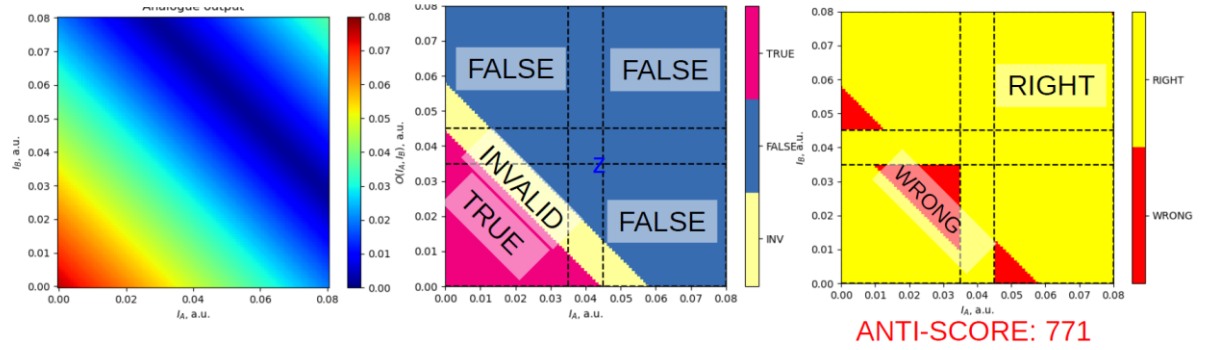

Figure 9. Result of optimisation of the NOR gate for the case of identical input weights.

5. Examples of full micromagnetic modelling.

Based on the results of the phenomenological modelling, we have focused our full micromagnetic simulations on the NAND gate design from sub-section 4.1 and assuming magnetic parameters extracted from fitting the experimental data acquired from the best MFPR produced previously. The results are presented below, along with those for a corresponding AND gate.

5.1 Micromagnetic modelling of a NAND gate.

The best (so far) results for a magnonic NAND gate are shown in Fig. 10 with the corresponding values of the logic level thresholds. A reasonable performance is observed, especially considering that these computationally heavy calculations do not allow one to use advanced optimisation tools.

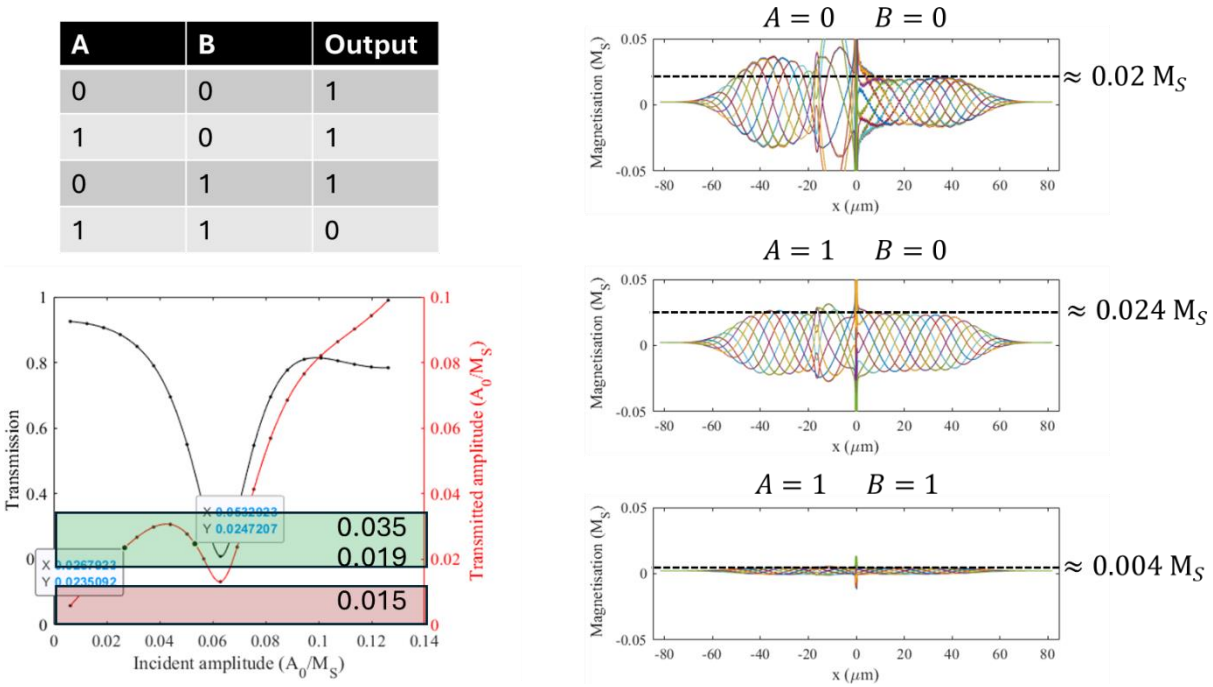

Figure 10. Results of full micromagnetic modelling for a magnonic NAND gate based on the MFPR experimentally implemented previously and data from which were used in validation of the phenomenological model in deliverable D2.3.

5.2 Micromagnetic modelling of an AND gate.

For a comparison, we show in Fig. 11 results of full micromagnetic modelling for an AND gate built upon the same MFPR as that used in Fig. 10. Again, a reasonable performance is observed.

A	B	Output
0	0	0
1	0	0
0	1	0
1	1	1

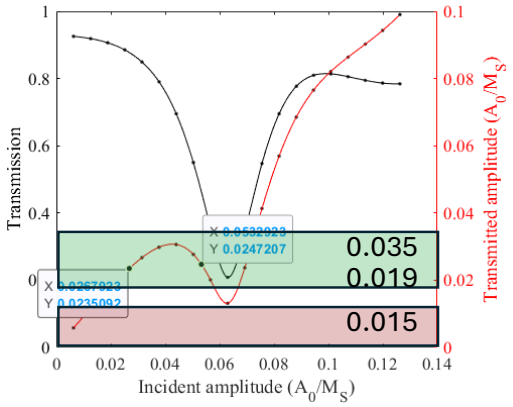

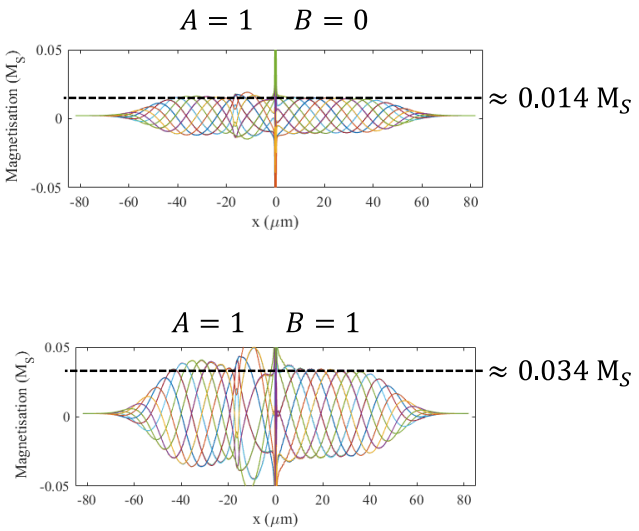

Figure 11. Results of full micromagnetic modelling for a magnonic AND gate based on the MFPR experimentally implemented previously and data from which were used in validation of the phenomenological model in deliverable D2.3.

6. Final remarks

In summary, we have designed a series of CMLG based on single CMRs or MFPRs and developed a phenomenological model that can be used for their optimisation. The best results are obtained for a magnonic NAND gate, which were further confirmed by full-scale micromagnetic simulations for a designed based on a realistic MFPR. Further optimisation of the designs will be done once feedback from their experimental implementation will be obtained.

---

1 H. Qin, R. B. Holländer, L. Flajšman, F. Hermann, R. Dreyer, G. Woltersdorf, and S. van Dijken, "*Nanoscale magnonic Fabry-Pérot resonator for low-loss spin-wave manipulation*", Nat. Commun. **12**, 2293 (2021).

2 A. Lutsenko, K. G. Fripp, A. V. Shytov, L. Flajšman, V. V. Kruglyak, and S. van Dijken, "*Magnonic Fabry-Perot resonators as programmable phase shifters and energy concentrators*", to be presented at "Neuromorphic Magnonics" workshop (Paris, 24-26 April 2024).

3 K. G. Fripp, Y. Au, A. V. Shytov, and V. V. Kruglyak, "*Nonlinear chiral magnonic resonators: Toward magnonic neurons*", Appl. Phys. Lett. **122**, 172403 (2023).